Title:

Experimental determination and mathematical modeling of standard shapes of forming autophagosomes

Yuji Sakai[1,2,3*], Satoru Takahashi[1,4], Ikuko Koyama-Honda[1], Chieko Saito[1], and Noboru Mizushima[1*]

[1]Department of Biochemistry and Molecular Biology, Graduate School of Medicine, The University of Tokyo, Bunkyo-ku, Tokyo 113-0033, Japan

[2]Department of Biosystems Science, Institute for Life and Medical Sciences, Kyoto University, Sakyo-ku, Kyoto 606-8507, Japan

[3]Interdisciplinary Theoretical and Mathematical Sciences (iTHEMS) Program, RIKEN, Wako, Saitama 351-0198, Japan

[4]Department of Neurosurgery, Tokyo Medical and Dental University, Bunkyo-ku, Tokyo 113-8510, Japan

*Correspondence: yuji-sakai@m.u-tokyo.ac.jp and nmizu@m.u-tokyo.ac.jp.

Summary

Autophagy is an intracellular degradation process mediated by autophagosomes. The formation of autophagosomes involves dynamic morphological changes of the precursor phagophore, in which a disk-shaped membrane cisterna grows, bends into a cup-shaped intermediate, and finally becomes a spherical autophagosome. However, the physical mechanism behind these morphological changes remains elusive. This is in part because the shapes of phagophores (i.e., forming autophagosomes) are highly variable, and their standard shapes have not been characterized precisely. Here, we first determined the average shapes of phagophores by statistically investigating three-dimensional electron micrographs of more than 100 phagophores. The results showed that the cup-shaped structures adopted a characteristic morphology; they were longitudinally elongated, and the rim was catenoidal with an outwardly recurved shape. From the characteristic shape of the rim, we estimated the Gaussian modulus that determines the elastic properties of the phagophore membrane. Using the Gaussian modulus, we established a theoretical model of the shape of entire phagophores. The model quantitatively reproduced the average morphology observed by electron microscopy and revealed that the characteristic shape of phagophores (i.e., an elongated shape with a catenoidal rim) was primarily determined by the relative size of the open rim to the total surface area. These results

suggest that autophagosomal membranes are highly flexible and that the morphological changes during autophagosome formation follow a stable path determined by elastic bending energy minimization.

Significance statement

Autophagy is an intracellular degradation process mediated by autophagosomes. The formation of autophagosomes involves dynamic morphological changes; a disk-shaped membrane cisterna grows, becomes a cup-shaped structure, and finally develops into a spherical autophagosome. However, since these characteristic morphological changes have never been quantitatively described, the physical mechanism behind these morphological changes remains elusive. Here, we determined the average shapes of forming autophagosomes by statistically investigating three-dimensional electron microscopy images and showed that the rim is catenoidal. Next, we established a theoretical model based on the elastic bending energy, which quantitatively reproduced the experimental results. These results suggest that autophagosomal membranes are highly flexible, and the characteristic morphological changes are primarily determined by elastic bending energy minimization.

Introduction

Eukaryotic cells have membranous organelles with a variety of characteristic shapes. The autophagosome, which mediates macroautophagy (hereafter simply referred to as autophagy), is unique among the various organelles in that its generation involves characteristic membrane deformation. Autophagy is a bulk degradation process, through which a portion of the cytoplasm is sequestered into autophagosomes and is degraded upon fusion with lysosomes (Figure 1) (Mizushima et al. 2011). In this process, a flat cisterna called a phagophore (also called an isolation membrane) grows from an initial disk through a cup-shaped intermediate and into a spherical stomatocyte. After the closure of the edge, it becomes a double-membrane autophagosome. Despite these characteristic morphological changes, there have been no systematic and quantitative studies to date on the standard morphology of phagophores during autophagosome formation. The morphology of phagophores is often approximated as a simple geometric shape, such as a part of a sphere or an ellipsoid, but the complexity and diversity of their morphology remain largely unexplored.

Quantitative and theoretical analyses can elucidate the mechanisms that control organelle morphology. Quantitative comparisons between experimentally observed and theoretically calculated shapes provide a mesoscopic, molecular-level explanation of the mechanisms that control organelle morphology (Bassereau et al. 2018, Lipowsky 1991, Ramakrishnan et al. 2014). In theoretical analyses, organelles are often considered to be simple geometric shapes, such as spheres or tubes, and their complex and diverse morphologies, and thus the mechanisms behind them, are often ignored. Although theoretical research on autophagy is only in its early phase, the morphology of phagophores has been analyzed by approximating parts of a sphere or an ellipse (Knorr et al. 2012, Sakai et al. 2020). However, the actual morphology of phagophores observed in cells is more complex, and previous studies have oversimplified their morphology.

In the present study, we statistically and quantitatively investigated the morphology of phagophores. First, we determined the average morphology of more than 100 phagophores obtained from three-dimensional (3D) electron micrographs. The results showed that phagophores were elongated vertically, with a rim curved outward to form a catenoid-like shape. Based on the characteristic shape of the rim that we observed experimentally, we estimated the physical parameters (i.e., line tension and Gaussian modulus) that determine the elastic properties of the phagophore membrane. Using these

parameters, we developed a theoretical model based on the elastic bending energy. The resulting theoretical model quantitatively reproduced the morphology during autophagosome formation observed by electron microscopy. These results suggest that autophagosomal membranes are highly flexible and that the characteristic shapes of phagophores are primarily determined by elastic bending energy minimization.

Results and Discussion

Quantification of phagophore morphology from 3D-electron micrographs

To understand the standard shapes of phagophores, we determined the average morphology of phagophores in mouse embryonic fibroblasts by array tomography, a technique that can be used in 3D electron microscopy (Micheva et al. 2007). Images of more than 100–200 serial sections (25-nm thickness) of a region containing several cells were captured using a scanning electron microscope. We collected 117 entire 3D structures of phagophores from 23 chemically fixed cells (Figure 2*A*). Next, each phagophore membrane was segmented and approximated as a point cloud $\{\vec{X}_i\}$ where each point $\vec{X}_i$ represented the location of a single point on the membrane of the i-th phagophore structure (Figure 2*B*). Cells were fixed with reduced osmium tetroxide to keep the inner and outer membranes attached to each other, which is their natural physiological state; if conventional osmium tetroxide had been used, the space between the outer and inner membranes would have been artificially expanded (Uemura et al. 2014). Thus, the inner and outer membranes were treated as a single membrane in each point cloud representation. Each 3D morphology was constructed by stacking a set of points obtained from a series of images (Figure 2*C*).

To obtain an average shape of structures with different sizes, we normalized the size of each 3D phagophore using standard *z*-score normalization, assuming that morphology is not size dependent. In *z*-score normalization, each point $\vec{X}_i$ was converted to a standardized point $\vec{Y}_i$ as

$$\vec{Y}_i = \frac{\vec{X}_i - \vec{\mu}_X}{\sigma_X}, \qquad \vec{\mu}_X = \frac{1}{N}\sum_{i=1}^{N} \vec{X}_i, \qquad \sigma_X = \sqrt{\frac{1}{N}\sum_{i=1}^{N} \left|\vec{X}_i - \vec{\mu}_X\right|^2}, \tag{1}$$

where $\vec{\mu}_X$, σ_X, and N represent the mean, deviation, and number of the points belonging to the point cloud, respectively. Then, the normalized point cloud $\{\vec{Y}_i\}$ was obtained.

Because phagophores in the electron microscopy images were oriented in various directions, we rotated each structure to be oriented in a uniform direction (along the *z*-axis). The average edge vector of a normalized point cloud, $\vec{\mu}_e$, was used as the orientation of each structure and was obtained as

$$\vec{\mu}_e = \frac{1}{M} \sum_{i \in edge}^{M} \vec{Y}_i, \tag{2}$$

where the point edges belonging to the cloud were summed and M was the number of edge points. From the average edge vector, the polar angle, θ_e, and azimuth angle, φ_e, of the structure were determined. Each point $\vec{Y}_i$ was rotated according to

$$\vec{Z}_i = R_y(-\theta_e) R_z(-\varphi_e) \vec{Y}_i, \tag{3}$$

where R_y and R_z are the matrices that rotate $\vec{Y}_i$ by $-\theta_e$ about the *y*-axis and $-\varphi_e$ about the *z*-axis, respectively, and then, a point cloud with uniform size and orientation, $\{\vec{Z}_i\}$, was obtained. The surface was constructed from the normalized point cloud by Delaunay triangulation (Figure 2*D* and Video S1). Thus, we reconstructed the normalized shapes of phagophores obtained from the 3D electron micrographs.

Because the obtained shapes of phagophores were diverse (reflecting the morphological changes during autophagosome formation), we selected four representative categories based on the rim size. The rim size σ_e was expressed as the magnitude of the deviation of the normalized point cloud belonging to the rim as

$$\sigma_e = \sqrt{\frac{1}{M} \sum_{i=1}^{M} \left| \vec{Y}_i - \vec{\mu}_e \right|^2}. \tag{4}$$

The four categories of observed shapes were as follows: disk ($\sigma_e > 1.1$), early-cup ($0.8 < \sigma_e < 1.0$), middle-cup ($0.5 < \sigma_e < 0.7$), and late-cup ($\sigma_e < 0.4$) (examples of 3D electron micrographs of each category are shown in Supplemental Figure S1). The point clouds in each category were superposed (Figure 3*A*–*D*, Video S2–5). The spread of the point clouds indicated the variation within each morphology, while the regions with a high density of points represented the modal morphology. Although individual phagophores were not axisymmetric, probably owing to deformation caused by

intracellular fluctuations, the superimposed point clouds appeared to be axisymmetric around the *z*-axis.

Thus, these point clouds were projected onto the radial and axial planes (Figure 3*E-H*). The average morphology obtained suggested that the cup-shaped phagophores had two characteristic features. First, they were elongated vertically along the rotation axis. This result was consistent with our previous observations by fluorescence microscopy (Tsuboyama et al. 2016). Second, as the phagophore membrane approached the rim, it curved inward and then outward, forming a catenoid shape. The outward curvature was higher in late-cups. However, the rim appeared to be straight and not curved outward in disks. These characteristic features were also observed in individual phagophores in electron micrographs (Figure3*I-L*).

One methodological concern was that these characteristic shapes might have resulted from chemical fixation of cells during sample preparation for electron microscopy. To rule out this possibility, we directly observed phagophores in live cells expressing GFP-LC3, a marker for phagophores and autophagosomes. Typical shapes of elongated phagophores with a catenoidal rim, which were consistent with the superimposed electron microscopy data, were frequently observed (Figure3*M-P*, Supplemental Figure S2). Thus, the structures observed by electron microscopy should represent the actual morphology of those in live cells.

To determine the average shape and quantify the curvature of the membrane, the projected point clouds were fitted with the *z*-axis symmetric polynomial function

$$x^2 = az^3 + bz^2 + cz + d, \tag{5}$$

where the fitting parameters are summarized in Table 1 (Figure 4*A-D*). The standard error of each parameter in the three cup shapes was within a few percentage points, while the error of the disk shape was larger because of the small number of statistics and the large classification range ($\sigma_e > 1.1$). Each fitting curve well reproduced the point clouds that were experimentally obtained by electron microscopy. The fitted curves of middle- and late-cups clearly had a catenoidal rim (curved outward). The 3D surface in the axisymmetric approximation was represented using the fitting function

$$(f(v)\cos u, f(v)\sin u, v), \qquad f(v) = \sqrt{av^3 + bv^2 + cv + d}, \tag{6}$$

where u represents the azimuth angle. The total curvature J (indicated by the line color in Figure 4*A-D*) on the surface at $z = v$ was obtained by

$$J(v) = J_m + J_p, \qquad J_m = -\frac{f''(v)}{[(f'(v))^2 + 1]^{3/2}}, \qquad J_p = \frac{1}{f(v)[(f'(v))^2 + 1]^{1/2}}, \quad (7)$$

where J_m and J_p represent the meridional (i.e., perpendicular) and parallel curvature relative to the *xy*-plane, respectively (Figure 4*E*, line colors in Figure 4*F*-*I*). In middle- and late-cups, the parallel curvature, J_p, increased, with a positive sign as the surface approached the rim from the bottom, while the meridional curvature, J_m, decreased, with a negative sign. Thus, the two orthogonal curvatures J_m and J_p had opposite signs and seemed to cancel each other out, thus reducing the total curvature J.

Estimation of the Gaussian modulus and line tension with phagophore growth

Each shape of the phagophore membrane shown in Figure 3 (i.e., disc, early-, middle-, and late-cups) is stable for several minutes during autophagosome formation (Tsuboyama et al. 2016, Sakai et al. 2020). Because this timescale (minutes) is sufficiently longer than the mechanical relaxation timescale (milliseconds) of the membrane, each morphology was considered to be in a stable equilibrium state (Sakai et al. 2020). Therefore, the forces acting on the rim were considered to be balanced, and thus several important physical quantities that characterize phagophore membranes can be extracted from the morphology by the force balance condition at equilibrium.

According to the elastic bending energy model interpreted in terms of stresses (Evans et al. 1980), the membrane can develop a meridional bending moment $M_m = \kappa_b J + \kappa_G J_p$; the first and second terms in this equation are associated with the total curvature, $J = J_m + J_p$, and the Gaussian curvature, $K = J_m J_p$, respectively (Figure 5*A*), while κ_b and κ_G represent the bending and the Gaussian moduli, respectively, which characterize the elastic properties of the membrane. As shown in the electron micrographs (Figure 3 and S.1), the phagophore had closely juxtaposed inner and outer membranes (*a* and *b* in Fig. 5*A*) with the same curvatures, and the rim can be approximated as a line (*c* in Fig. 5*A*). The spontaneous curvature was assumed to be zero because the outer and inner membranes had the same elastic properties. Because the phagophore rim was not exposed to any external rotational moment, the total moment should be zero, that is, $M_m = 0$. From this moment balancing condition, the Gaussian modulus can be obtained as

$$\frac{\kappa_G}{\kappa_b} = -\frac{J}{J_p}. \quad (8)$$

Meanwhile, the membrane can develop transverse a shear force $F_m = d(x_r M_m)/ds - M_p dx_r/ds$, with a rim radius x_r, arclength s, and parallel moment $M_p = \kappa_b J + \kappa_G J_m$.

To resist the shear force $2F_m$ from the two membranes (inner and outer membranes), line tension λ must act at the rim (Figure 5*A*). From the shear force balancing condition, $2F_m + \lambda \sin\theta_r = 0$, the line tension at the rim can be obtained as

$$\lambda = -\frac{2x_r}{\sin\theta_r}\left(\kappa_b \frac{dJ}{ds} + \kappa_G \frac{dJ_p}{ds} + \kappa_G \frac{J_p - J_m}{x_r}\cos\theta_r\right), \tag{9}$$

where θ_r represents the tilt angle at the rim. Therefore, the Gaussian modulus, κ_G, and line tension, λ, are determined by fitting the experimental phagophore membrane shapes (Figure 4), where the curvatures are obtained from Equation (7).

The Gaussian modulus obtained by fitting the experimental phagophore membrane shapes with a polynomial function was $-(0.21 \pm 0.05)\kappa_b$, with no significant differences among the disc, early-, middle-, and late-cups (Figure 5*B*). The deviation σ_X defined in Equation (1), which represents the spatial extent of the point clouds of each morphology (Figure 3), was used as a unit of length (Supplemental Figure S5). The obtained values of the phagophore membrane were within the reported range of biological membranes, namely, $-\kappa_b < \kappa_G < 0$ (Siegel et al. 2004, Hu et al. 2012).

The line tension λ, obtained by fitting the experimental phagophore membrane shapes, had positive values and increased with the membrane area (changing from disk to early-, middle-, and late-cup shapes) (Figure 5*C*). The obtained value was smaller than the typical value of the motor tractive forces causing membrane tubulation (~ 10 pN) (Koster et al. 2003) and was comparable to the forces of actin polymerization (~ 1 pN) (Footer et al. 2007). Positive line tension indicates an inward lateral force acting on the rim, which is opposed to the outward bending force acting to flatten the inner and outer membranes. These data suggest that the cup shape in the intermediate state is stable because the inward line tension of the rim and outward bending elasticity of the inner and outer membranes are balanced.

Modeling of phagophore morphology

Next, to investigate whether the morphological features of the phagophores obtained by electron microscopy were reasonable, we conducted a mathematical model analysis. In the elastic bending energy model, the free energy F was given by

$$F = \int \left(\frac{\kappa_b}{2}J^2 + \kappa_G K\right) dA + \gamma_A A + \gamma_L L. \tag{10}$$

Here, the first term is the elastic bending energy with the total curvature, $J = J_m + J_p$, and Gaussian curvature, $K = J_m J_p$ (Helfrich 1973), of the inner and outer membranes. The second and third terms are the constraints for the membrane area A and the rim length L, respectively, while γ_A and γ_L are the Lagrange multipliers for A and L, respectively. The phagophore was assumed to have closely juxtaposed inner and outer membranes with the same curvature and area, and the rim was approximated as a closed line (Figure 5*A*). The bending modulus is $\kappa_b = 20 k_B T$ with the Boltzmann constant k_B and temperature T. The Gaussian modulus obtained from the experiment, $\kappa_G = -0.2\kappa_b$, was used (Figure 5*B*). For an axisymmetric membrane, the free energy was rewritten as

$$F = 2\pi \int_0^{s_1} \left[\frac{\kappa_b}{2} x \left(J_m + J_p \right)^2 + \kappa_G x J_m J_p + \gamma_A x + \gamma_L \dot{x} \right] ds\,, \tag{11}$$

with

$$J_m = \dot{\theta}, \qquad J_p = \frac{\sin\theta}{x}, \tag{12}$$

where s, s_1 x, and θ are the arc length, location of the rim, radial coordinate, and tilt angle, respectively (Figure 5*A*). The dots represented the derivative with respect to s. The membrane morphology was obtained by the variational method (Tu et al. 2003, Tu 2010). A complete method for obtaining the morphology from the bending energy is described in the Supplemental Information.

First, we determined the morphology of a stable cup-shaped membrane with several different rim radiuses (Figure 6*A-D*). Because the free energy and the stable membrane morphology are scale invariant, the rim radius was rescaled as

$$l = x_r / \sqrt{A/2\pi}\,, \tag{13}$$

with membrane area $A = 4\pi \int_0^{s_1} x ds$ and rim radius $x_r = \int_0^{s_1} \cos\theta\, ds$, where $l = 1$ represents a flat disk shape and $l = 0$ a closed sphere shape. Cups for which $0.2 < l < 0.6$ were not spherical but elongated vertically along the rotational axis. This trend was also observed in our previous models (Sakai et al. 2020). In these structures, the curvature in the elongated direction was reduced, thus lowering the bending energy (a cylinder [radius r, height h] had less bending energy than a spherical cap [radius r] of the same area when $r > h$). Furthermore, these structures had a catenoid-like rim. As the rim radius became smaller, the warping became stronger. These morphological features obtained by the theoretical model were consistent with those obtained by electron microscopy (Figure 3). Note that γ_A was always negative (Figure 6*A-D*), which indicates that membrane area growth decreased the energy of cup shapes (see Equation 10).

Next, we calculated the total curvature to quantitatively evaluate the shapes obtained by the theoretical model (Figure 6*A-D*). In all structures, from a disc to a cup, the total curvature was reduced near the rim. The meridional curvature, J_m, and parallel curvature, J_p, were also calculated (Supplemental Figure S3). The meridional curvature was negative near the rim, reflecting the outward curvature of the membrane, while the parallel curvature was positive. As a result of the two competing curvatures, negative and positive, the total curvature near the rim seemed to be smaller. Except for the rim, which was isotropic, the two curvatures were of approximately the same magnitude.

We further investigated the change of the curvatures during the morphological transition from a disc to a cup (Figure 6*E*). As the rim radius decreased, the parallel curvature J_p at the rim increased monotonically because the curvature given by $J_p = \sin\theta / x$ was approximately inversely proportional to the radial distance x. In the middle- and late-cup shapes, the surface near the rim got closer to the rotational axis, and therefore the parallel curvature, J_p, increased. On the other hand, as the rim radius decreased, the meridional curvature, J_m, decreased (became more negative) in opposition to the parallel curvature, J_p, keeping the total curvature ($J = J_m + J_p$) small. Thus, the two orthogonal curvatures canceled each other out, making the rim catenoidal.

Comparison between theoretical and experimental morphologies

We compared the results of our theoretical calculations with our experimental data. The point clouds obtained from electron micrographs (Figure 3*E-H*) were superimposed on the theoretically calculated morphologies with the same rim sizes (Figure 7). At each step, the experimental and theoretical results overlapped well. In particular, the longitudinally elongated shape and the catenoidal rim were well captured by the theoretical calculations. The relative error of the theoretical curves to the experimental fitting curves was within 30% across all shapes (Supplemental Figure S4). The magnitude of this error was $\sim k_B T$ in energy, which was within the range of thermal fluctuations. These results suggest that the morphological transition of phagophores during autophagosome formation follows a stable path determined by the elastic bending energy.

However, there was a slight discrepancy between the theoretical expectation and experimental data, especially at the late-cup stage (Figure 7). This discrepancy may be partially explained by non-equilibrium fluctuations. The outer and rim membranes of the

phagophore often attach to the endoplasmic reticulum (Hayashi-Nishino et al. 2009, Ylä-Anttila et al. 2009, Uemura et al. 2014), and the phagophore membrane may actively fluctuate like the endoplasmic reticulum membrane. Cytoskeletons may also contribute to autophagosome shaping (Mi et al. 2015, Kast et al. 2015). Another possibility is the influence of lipid asymmetry. During autophagosome formation, lipids are provided to the outer leaflet by the lipid transfer protein ATG2 (Maeda et al. 2019, Osawa et al. 2019, Valverde et al. 2019). Although it is hypothesized that the autophagosomal scramblase ATG9 resolves lipid asymmetry (Matoba, et al. 2020), the remaining asymmetry may contribute to the elongation of phagophores (Seifert et al. 1991). However, these effects on the shape of the phagophore would be within the range of thermal fluctuation.

Conclusion

The shape of phagophores has been empirically assumed, but their standard shapes have not yet been determined experimentally. In this study, we quantitatively analyzed the average morphology of phagophores using 3D electron microscopy data and found that phagophores are vertically elongated and that their rims have a catenoidal shape. We also showed that these characteristic features could be well explained by an elastic bending energy model. These results suggest that phagophore membranes are highly flexible and the morphological changes during autophagosome formation follow a stable path determined by elastic bending energy minimization. Our results also suggest that the shape of phagophores is primarily determined by the relative size of the open rim to the total surface area without any external influences. We do not rule out the possibility that some internal forces (e.g., lipid asymmetry) or external forces (e.g., exerted by the endoplasmic reticulum or cytoskeletons) influence the phagophore morphology, but these effects would be relatively minor. Furthermore, our model predicts that the line tension on the phagophore rim increases with membrane growth, which means that the contractile force applied to the rim increases. The model also predicts that a larger membrane area is energetically more stable for the cup shapes. This stability could be one of the mechanisms underlying the directional lipid transfer from the endoplasmic reticulum to phagophores during phagophore growth.

Methods

All methods can be found in the accompanying Transparent Methods supplemental file.

Acknowledgments

This work was supported by a Grant-in-Aid for Scientific Research (KAKENHI) from JSPS (20K06482 to Y.S., 22H04635 to I. K-.H., and 22H04919 to N.M.) and Exploratory Research for Advanced Technology (ERATO; grant number JPMJER1702) from the Japan Science and Technology Agency (JST) (to N.M.). The numerical computations have been performed with the RIKEN supercomputer system (HOKUSAI). We would like to thank Michael M. Kozlov for useful discussions.

Author Contributions

Conceptualization, Y.S. and N.M.; Methodology, Y.S.; Investigation, Y.S., S.T., C.S., and I.K-.H.; Formal analysis, Y.S.; Writing, Y.S., I.K-.H., and N.M.; Visualization, Y.S., S.T., C.S., and I.K-.H.; Funding acquisition, Y.S. and N.M.; Resources, Y.S., S.T., C.S., and I.K-.H.; Supervision, Y.S. and N.M.

Declaration of Interests

The authors declare no competing interests.

References

P. Bassereau, et al., The 2018 biomembrane curvature and remodeling roadmap. J. Phys. D. Appl. Phys. 51, 343001 (2018).

E. A. Evans, R. Skalak, Mechanics and Thermodynamics of Biomembranes (CRC Press, 2018) https:/doi.org/10.1201/9781351074339.

M. J. Footer, J. W. J. Kerssemakers, J. A. Theriot, M. Dogterom, Direct measurement of force generation by actin filament polymerization using an optical trap. Proc. Natl. Acad. Sci. U. S. A. 104, 2181–2186 (2007).

M. Hayashi-Nishino, et al., A subdomain of the endoplasmic reticulum forms a cradle for autophagosome formation. Nat. Cell Biol. 11, 1433–1437 (2009).

W. Helfrich, Elastic properties of lipid bilayers: theory and possible experiments. Z. Naturforsch. C. 28, 693–703 (1973).

395 M. Hu, J. J. Briguglio, M. Deserno, Determining the Gaussian curvature modulus of lipid
396 membranes in simulations. Biophys. J. 102, 1403–10 (2012).

397 D. J. Kast, A. L. Zajac, E. L. F. Holzbaur, E. M. Ostap, R. Dominguez, WHAMM Directs
398 the Arp2/3 Complex to the ER for Autophagosome Biogenesis through an Actin Comet
399 Tail Mechanism. Curr. Biol. 25, 1791–1797 (2015).

400 R. L. Knorr, R. Dimova, R. Lipowsky, Curvature of Double-Membrane Organelles
401 Generated by Changes in Membrane Size and Composition. PLoS One 7, e32753 (2012).

402 G. Koster, M. VanDuijn, B. Hofs, M. Dogterom, Membrane tube formation from giant
403 vesicles by dynamic association of motor proteins. Proc. Natl. Acad. Sci. 100, 15583–
404 15588 (2003).

405 R. Lipowsky, The conformation of membranes. Nature 349, 475–481 (1991).

406 S. Maeda, C. Otomo, T. Otomo, The autophagic membrane tether ATG2A transfers lipids
407 between membranes. Elife 8 (2019).

408 K. Matoba, et al., Atg9 is a lipid scramblase that mediates autophagosomal membrane
409 expansion. Nat. Struct. Mol. Biol. 27, 1185–1193 (2020).

410 N. Mi, et al., CapZ regulates autophagosomal membrane shaping by promoting actin
411 assembly inside the isolation membrane. Nat. Cell Biol. 17, 1112–1123 (2015).

412 K. D. Micheva, S. J. Smith, Array Tomography: A New Tool for Imaging the Molecular
413 Architecture and Ultrastructure of Neural Circuits. Neuron 55, 25–36 (2007).

414 N. Mizushima, T. Yoshimori, Y. Ohsumi, The Role of Atg Proteins in Autophagosome
415 Formation. Annu. Rev. Cell Dev. Biol. 27, 107–132 (2011).

416 T. Osawa, et al., Atg2 mediates direct lipid transfer between membranes for
417 autophagosome formation. Nat. Struct. Mol. Biol. 26, 281–288 (2019).

418 N. Ramakrishnan, R. P. Bradley, R. W. Tourdot, R. Radhakrishnan, Biophysics of
419 membrane curvature remodeling at molecular and mesoscopic lengthscales. J. Phys.
420 Condens. Matter 30, 273001 (2018).

421 Y. Sakai, I. Koyama-Honda, M. Tachikawa, R. L. Knorr, N. Mizushima, Modeling
422 Membrane Morphological Change during Autophagosome Formation. iScience 23,
423 101466 (2020).

U. Seifert, K. Berndl, R. Lipowsky, Shape transformations of vesicles: Phase diagram for spontaneous- curvature and bilayer-coupling models. Phys. Rev. A 44, 1182–1202 (1991).

D. P. Siegel, M. M. Kozlov, The Gaussian Curvature Elastic Modulus of N-Monomethylated Dioleoylphosphatidylethanolamine: Relevance to Membrane Fusion and Lipid Phase Behavior. Biophys. J. 87, 366–374 (2004).

K. Tsuboyama, et al., The ATG conjugation systems are important for degradation of the inner autophagosomal membrane. Science (80-.). 354, 1036–1041 (2016).

Z. C. Tu, Compatibility between shape equation and boundary conditions of lipid membranes with free edges. J. Chem. Phys. 132, 084111 (2010).

Z. C. Tu, Z. C. Ou-Yang, Lipid membranes with free edges. Phys. Rev. E 68, 061915 (2003).

T. Uemura, et al., A Cluster of Thin Tubular Structures Mediates Transformation of the Endoplasmic Reticulum to Autophagic Isolation Membrane. Mol. Cell. Biol. 34, 1695–1706 (2014).

D. P. Valverde, et al., ATG2 transports lipids to promote autophagosome biogenesis. J. Cell Biol. 218, 1787–1798 (2019).

P. Ylä-Anttila, H. Vihinen, E. Jokitalo, E.-L. Eskelinen, 3D tomography reveals connections between the phagophore and endoplasmic reticulum. Autophagy 5, 1180–1185 (2009).

Figures

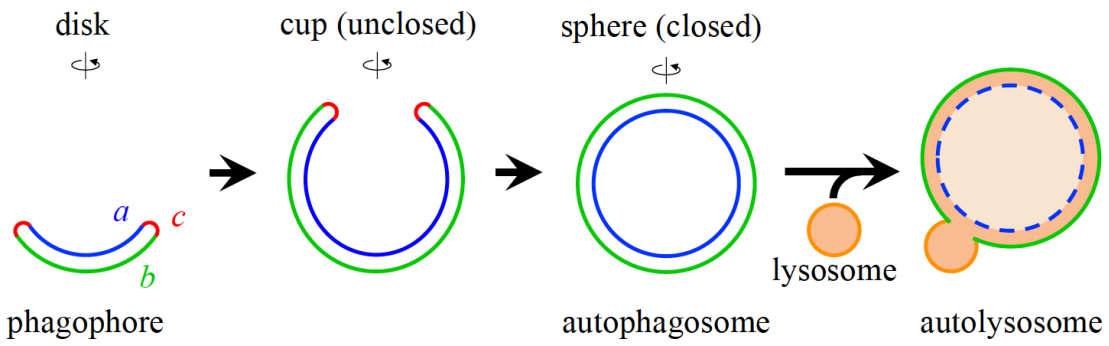

Figure 1. Schematic representation of autophagosome formation.
Each shape represents an axially symmetric membrane structure. As surface area increases, the shape of a forming autophagosome (phagophore) changes from an initial disk, through a cup-shaped intermediate, to a spherical closed autophagosome. The regions labeled *a*, *b*, and *c* correspond to the inner membrane, the outer membrane, and the rim, respectively. Eventually, autophagosomes and lysosomes fuse to degrade the contents of the former.

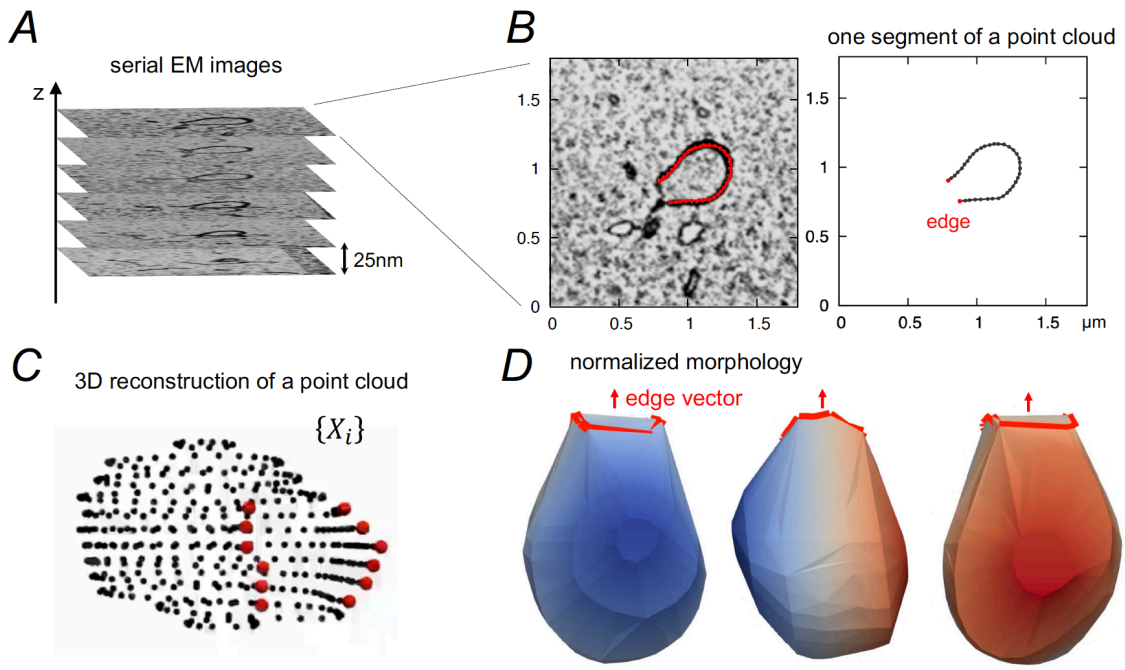

Figure 2. Three-dimensional electron microscopy (EM) of phagophores. (*A*) Serial EM images of a phagophore. (*B*) Left, an EM section image; the red dots represent the contour of the phagophore. Right, one segment of a point cloud of the extracted contour; the two red dots represent the edges of the phagophore. (*C*) 3D reconstruction of a point cloud. (*D*) A normalized shape of a phagophore, in which the deviation of the point cloud was normalized to one and rotated so that the direction of the edge aligns with the *z*-axis. Each structure is shown rotated 90 degrees about the *z*-axis. Rotating views (the *z*-axis is the rotation axis) are shown in Video S1. The surface was constructed by Delaunay triangulation in which the open edge of the cup (the area surrounded by the red line) was also considered as part of the surface.

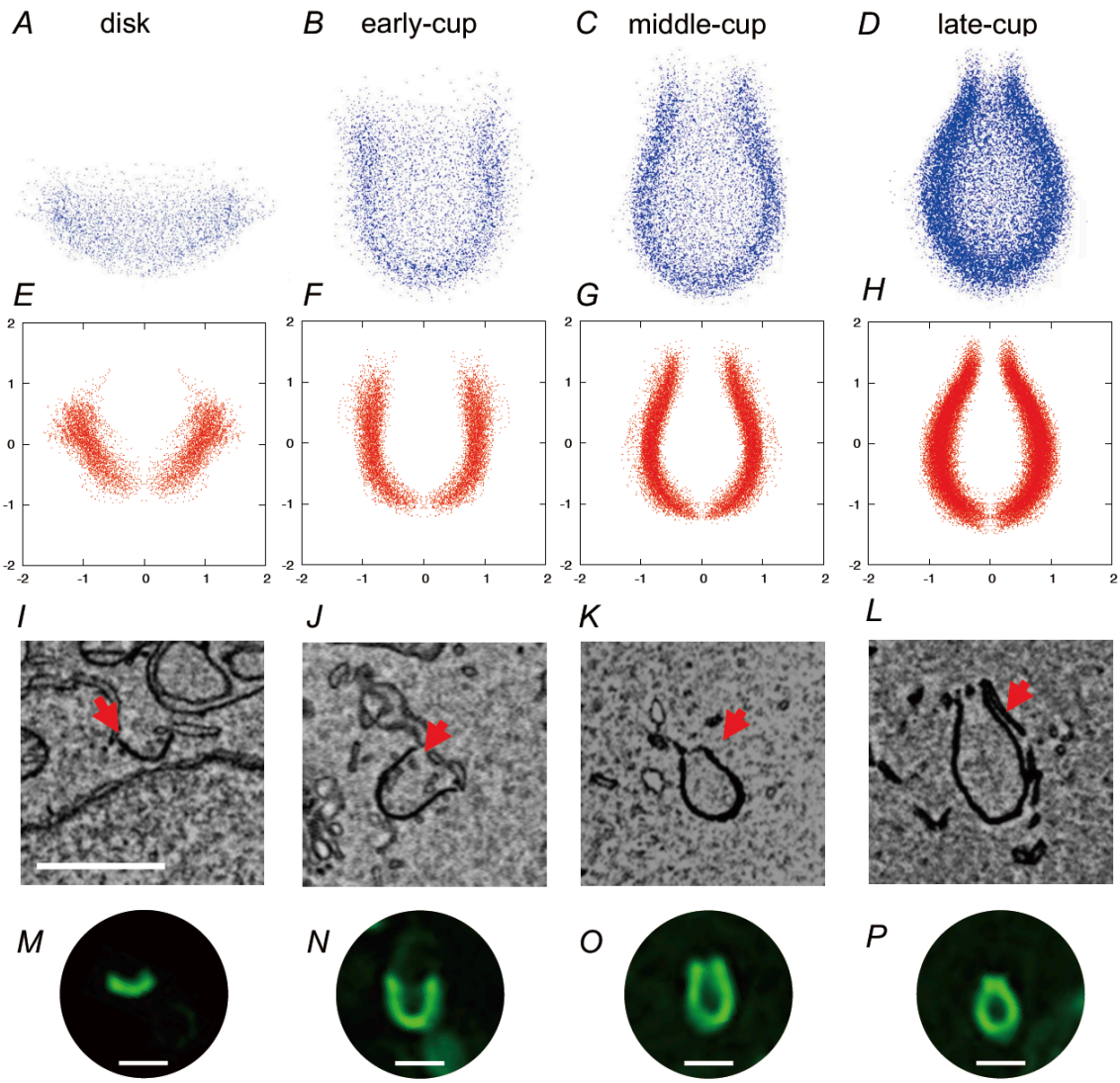

Figure 3. Average shape of phagophores.

(*A–D*) Three-dimensional point clouds of disks (*A*), early-cups (*B*), middle-cups (*C*), and late-cups (*D*) are shown. Point clouds were obtained from electron microscopy (EM) images of 15 disks (3,491 points), 16 early-cups (4,585 points), 24 middle-cups (8,578 points), and 45 late-cups (17,692 points) and then superposed. Rotating views (the *z*-axis is the rotation axis) are shown in Video S2–5. (*E–H*) The projected point clouds of disks (*E*), early-cups (*F*), middle-cups (*G*), and late-cups (*H*) onto the radial (*x*) and axial (*y*) plane. The unit of length was normalized so that the variance of the point set was one. (*I–L*) Examples of EM images of phagophores at the disk (*I*), early-cup (*J*), middle-cup (*K*), and late-cup (*L*) stages. The red arrows indicate phagophores; scale bar, 1 μm. (*M–P*) Examples of live-cell imaging of GFP-LC3 showing phagophores at the disk (*M*), early-cup (*N*), middle-cup (*O*), and late-cup (*P*) stages; scale bar, 1 μm.

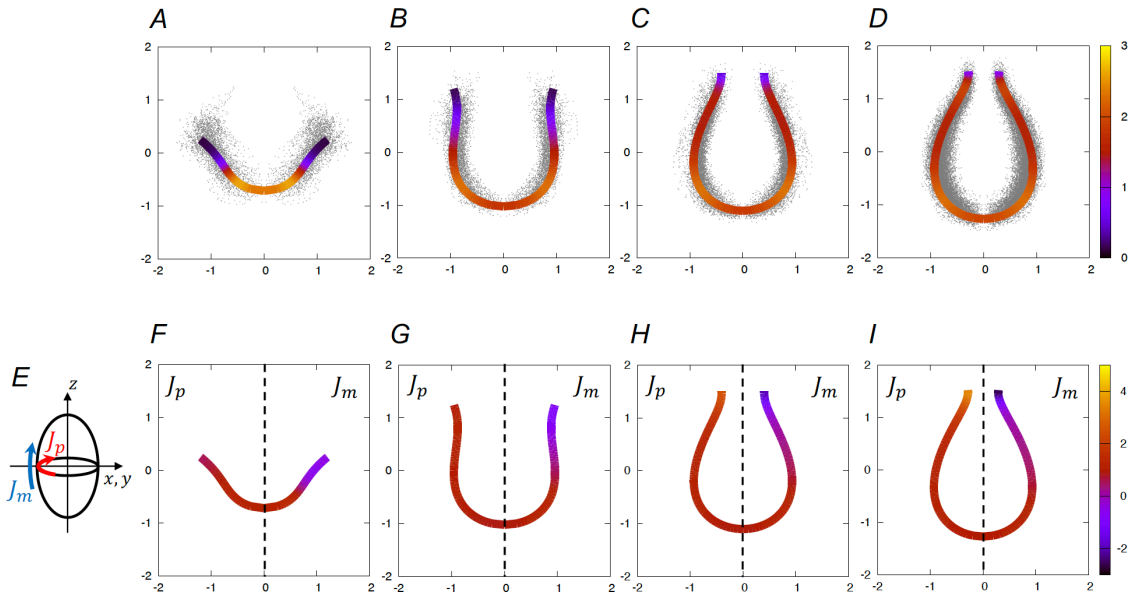

Figure 4. Shapes and curvatures fitted with approximate curves.
(*A–D*) The shapes fitted with polynomial functions of a disk (*A*), an early-cup (*B*), a middle-cup (*C*), and a late-cup (*D*), in which the line color represents the total curvature. In each panel, the black dots represent the same point set as in Figure 3*E–H*, respectively. The unit of length was normalized so that the variance of the point set was one. (*E*) A schematic description of the meridional and parallel curvatures relative to the *xy*-plane, J_m and J_p, respectively. (*F–I*) The meridional (J_m, $x \geq 0$, right) and parallel (J_p, $x \leq 0$, left) curvatures of a disk (*F*), an early-cup (*G*), a middle-cup (*H*), and a late-cup (*I*) are shown by the various line colors; the shape of the fitting curve in each panel is the same as those in panels *A–D*.

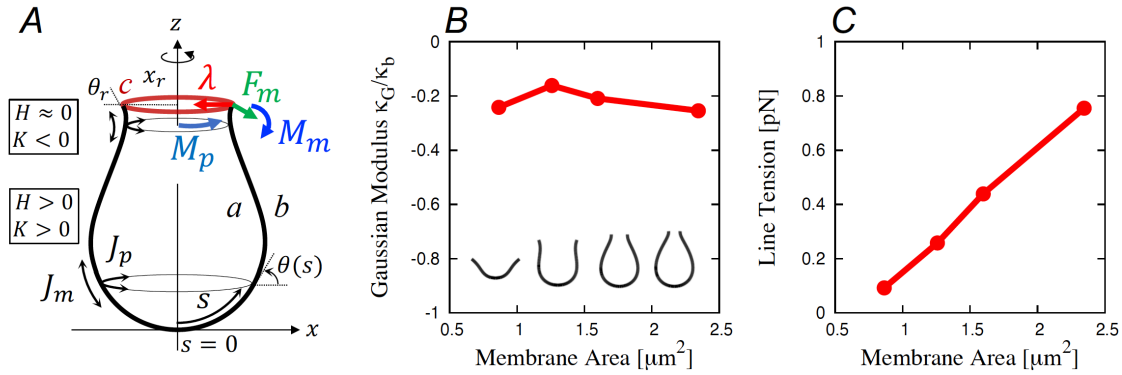

Figure 5. Gaussian modulus and line tension of growing phagophores.
(*A*) A schematic description of the forces acting on the rim of the axisymmetric membrane. z is the axis of symmetry, s is the length along the contour measured from the origin, and θ is the angle between the tangent to the contour and the x-axis. M_m and M_p are the meridional and parallel moments, respectively. F_m and λ are the transverse shear force and the line tension, respectively. J_m and J_p are the two principal curvatures. *a* and *b* represent the inner and outer membranes, respectively, and are shown overlapping in this figure. *c* represents the rim. J and K are the total and Gaussian curvatures, respectively, with $J > 0, K > 0$ for convex surfaces and $J \approx 0, K < 0$ for catenoidal surfaces. (B) Gaussian modulus obtained by fitting the experimental shapes, where $\kappa_b = 20k_BT$. (C) Line tension obtained by fitting the experimental shapes. The membrane area, $A = 4\pi \int f\sqrt{1 + (f')^2}dx$, is also obtained from the polynomial fitting.

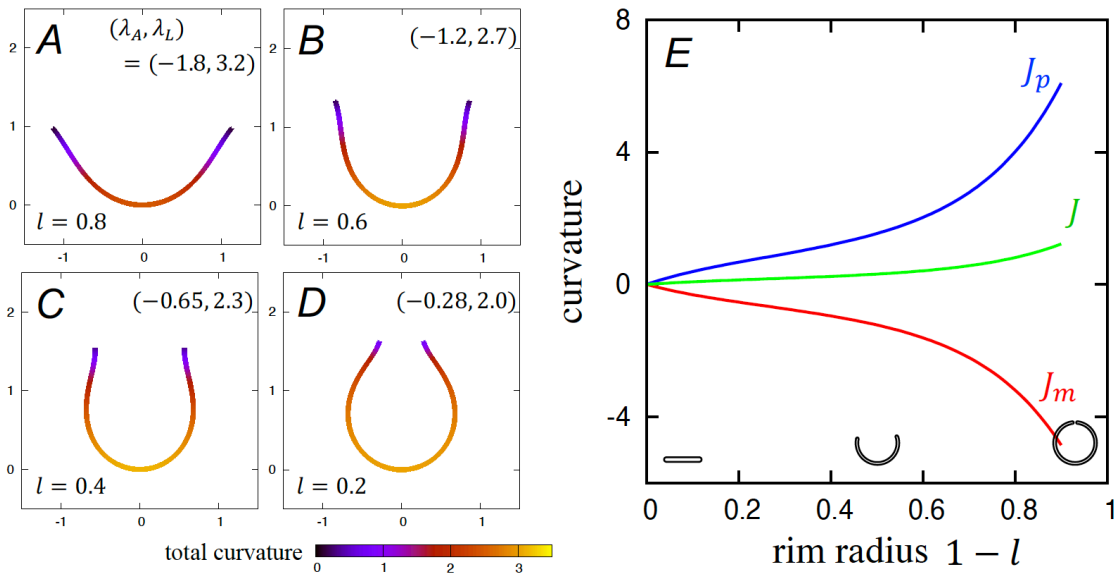

Figure 6. Shapes and curvatures obtained from theoretical calculations. (*A–D*) Membrane shapes obtained from the bending energy with Gaussian modulus $\kappa_G = -0.2\kappa_b$ for several values of the rim radius $l = 0.8$ (*A*), $l = 0.6$ (*B*), $l = 0.4$ (*C*), and $l = 0.2$ (*D*), where the line color represents the total curvature. (*E*) The meridional, parallel, and total curvatures, J_m (red), J_p (blue), and J (green), at the rim as a function of the rim radius l. The unit of length was non-dimensionalized by the length $\sqrt{A/4\pi}$.

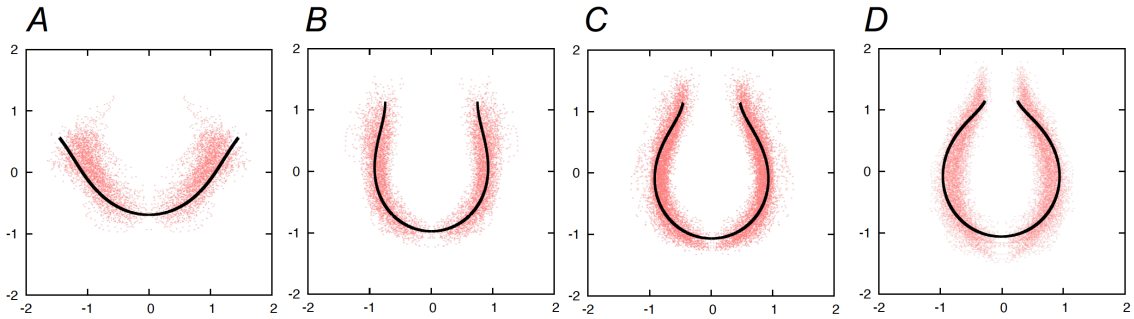

Figure 7. Comparison of theoretical and experimental shapes.

The theoretically calculated shapes (black lines) were superimposed over the experimentally obtained point clouds (red) and the fitting curves (gray lines) of disks (*A*), early-cups (*B*), middle-cups (*C*), and late-cups (*D*) (using the same data as shown in Figure 3 (*E*–*H*)). The theoretical results were normalized so that the mean of the point cloud representing each shape was zero and the variance was one, in the same way as the experimental results were normalized. The rim size σ_e was fixed at $\sigma_e = 1.45$ (*A*), 0.75 (*B*), 0.48 (*C*), and 0.28 (*D*), corresponding to $l = 0.8$, 0.39, 0.24, and 0.13, respectively.

Supporting Information

Elastic bending energy and shape equations of membranes

For an axisymmetric geometry, the free energy of the membrane was given by

$$F = 2\pi \int_0^{s_1} \left[\kappa_b x \left(\dot{\theta} + \frac{\sin\theta}{x} \right)^2 + 2\kappa_G \dot{\theta} \sin\theta + 2\gamma_A x + \gamma_L \dot{x} \right] ds\,, \qquad (S1)$$

where s, x, and θ are the arc length, radial coordinate, and tilt angle, respectively (Figure 5*A*) (Tu et al. 2003, Tu 2010); s_1 represents the location of the rim; κ_b and κ_G are the bending elastic moduli; and γ_A and γ_L are the Lagrange multipliers for the area A and the rim length L, respectively. The free energy should be minimized with the constraints $\dot{x} = \cos\theta$, and thus the action $S = 2\pi \int_0^{s_1} \mathcal{L} ds$ was constructed with the Lagrangian

$$\mathcal{L} = \kappa_b x \left(\dot{\theta} + \frac{\sin\theta}{x} \right)^2 + 2\kappa_G \dot{\theta} \sin\theta + 2\gamma_A x + \gamma_L \dot{x} + \gamma_x (\dot{x} - \cos\theta), \qquad (S2)$$

where γ_x is the Lagrange multiplier for $\dot{x}$. Based on variational theory (Tu 2010), the shape equation to determine the membrane shape with the minimum free energy is given by

$$\ddot{\theta} = -\frac{\tan\theta}{2}\dot{\theta}^2 - \frac{\dot{\theta}\cos\theta}{x} + \frac{\sin 2\theta}{2x^2} + \gamma_L \tan\theta + \frac{\tan\theta}{2}\left(\frac{\sin\theta}{x}\right)^2, \qquad (S3)$$

with the boundary conditions at the rim ($s = s_1$)

$$\left[\dot{\theta} + \left(1 + \frac{\kappa_G}{\kappa_b}\right) \frac{\sin\theta}{x} \right]_{s=s_1} = 0, \qquad (S4)$$

$$\left[-2\left(1 + \frac{\kappa_G}{2\kappa_b}\right) \kappa_G \left(\frac{\sin\theta}{x}\right)^2 + 2\gamma_L + \gamma_A \frac{\cos\theta}{x} \right]_{s=s_1} = 0. \qquad (S5)$$

These boundary conditions at the rim indicate that Gaussian curvature, line tension, and surface tension are obtained from the curvature at the rim. The initial conditions at $s = 0$ for x and θ are $x(0) = \theta(0) = 0$.

By solving the shape equation with the boundary conditions, a stable shape is obtained for a membrane area $A = 4\pi \int_0^{s_1} x ds$ and rim radius $x_r = \int_0^{s_1} \cos\theta\, ds$, with the corresponding Lagrange multipliers γ_A and γ_L, as shown in in Figure 6.

To compare theoretical expectations with the empirical data shown in Figure 7, the computed shapes were normalized in the same way as in the experiment. That is, we constructed a point cloud of axisymmetric 3D shapes from the 2D shapes obtained in the calculation and normalized them using *z*-score normalization (see Equations 1 to 4).

Cell culture

Mouse embryonic fibroblasts (MEFs) were cultured in Dulbecco's modified Eagle's medium (DMEM: D6546, Sigma-Aldrich) supplemented with 10% fetal bovine serum (172012, Sigma-Aldrich), and 2 mM L-glutamine (25030-081, Gibco) in a 5% CO_2 incubator. For the starvation treatment, cells were washed twice and incubated in amino acid-free DMEM (048-33575, Wako Pure Chemical Industries) without serum. MEFs that stably express GFP-LC3 were generated previously (Itakura and Mizushima, 2010)

Three-dimensional electron microscopy of phagophores using array tomography

A glass base dish was coated with carbon using a vacuum evaporator (IB-29510VET, JEOL) and then coated with 0.1% gelatin and dried under UV irradiation, as described previously (Maeda et al. 2020). Cells were cultured in the pretreated glass base dish for 2 days and starved for 30 min just before fixation. The cells were first fixed with 2.5% glutaraldehyde (G018/1, TAAB) in 0.1 M sodium cacodylate buffer, pH 7.4 (37237-35, Nacalai Tesque), overnight at 4ºC and then with 1% osmium tetroxide (3020-4, Nisshin EM) and 1.5% potassium ferrocyanide (161-03742, Wako) in 0.065 M sodium cacodylate buffer for 2 h at 4ºC. The fixed cells were washed five times with Milli-Q water, block-stained with 3% uranium acetate for 1 h, and dehydrated with an ethanol series. After a 1-h dehydration in 100% ethanol, the cells were embedded in Epon (EPON812, TAAB), polymerized at 40ºC for 12 h, and then polymerized at 60ºC for 48 h. Glass bases were removed from blocks by soaking them in liquid nitrogen, and then, the top surface of the blocks was trimmed to 100 × 100 μm using razor blades. To cut ultra-thin serial sections, we used a diamond knife with an ultra-jumbo boat (Ultrajumbo 45 degree, Diatome) mounted on an ultramicrotome (UC7, Leica). Serial 25-nm thick sections were cut, creating a ribbon of 130 serial sections, and collected onto a silicon wafer that was held and manipulated by a micromanipulator (Märzhäuser Wetzlar). Electron microscopic images were acquired using a scanning electron microscope (JSM7900F, JEOL) as described previously (Maeda et al. 2020).

588 In the 3D reconstruction, the scale factors in the stack direction were adjusted assuming
589 axisymmetry of phagophores as described previously (Hayashi-Nishino et al. 2009, Ylä-
590 Anttila et al. 2009) in order to compensate for the compression of the structures during
591 sample preparation (fixation and sectioning) for electron microscopy.
592
593 **Fluorescence microscopy**
594
595 MEFs stably expressing GFP-LC3B were subjected to live-cell fluorescence imaging
596 using a SpinSR10 spinning-disk confocal microscope (Olympus) equipped with an
597 ORCA-Flash 4.0 camera (Hamamatsu), a UPLAPO OHR 60× lens (NA 1.50, Olympus),
598 a 3.2× optical zoom lens, and a SORA disk in place (Yokogawa). The microscope was
599 operated with cellSens Dimension v2.3 (Olympus). During live-cell imaging, a dish was
600 mounted in a chamber (INUB-ONI-F2, TOKAI HIT) to maintain the incubation
601 conditions at 37ºC and 5% CO_2. Five slices with a thickness of 250 nm were acquired.
602 The images were processed with cellSens Dimension software using the following
603 settings: deconvolution with advanced maximum likelihood algorithm, 5× interaction,
604 adaptive PSF filter settings.
605
606
607 **Suppprting References**
608 E. Itakura, N. Mizushima, Characterization of autophagosome formation site by a
609 hierarchical analysis of mammalian Atg proteins. Autophagy 6, 764–776 (2010).
610

611 **Suppprting Figures**

612

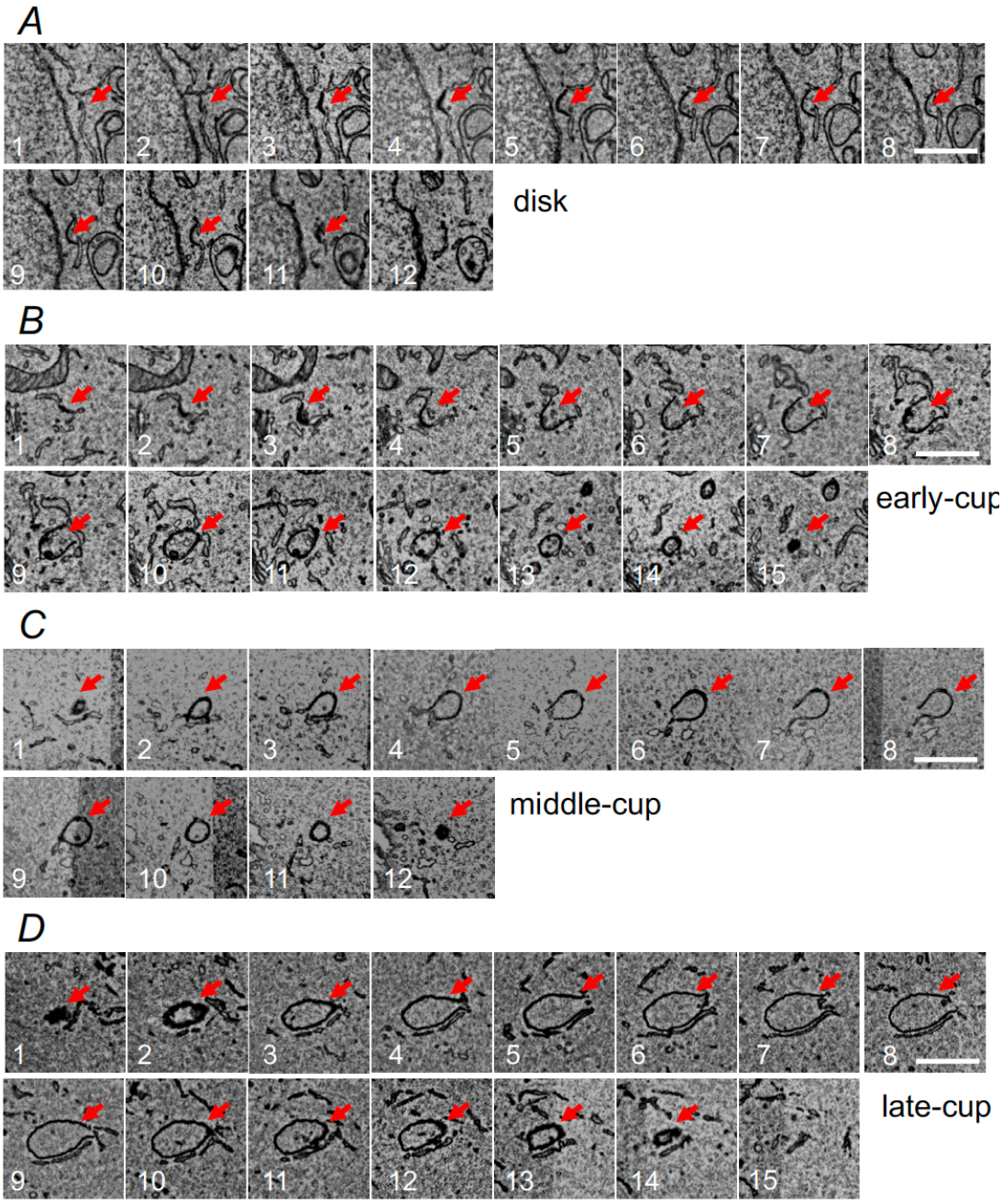

613

614 **Figure S1. Three-dimensional electron microscopy (EM) images of phagophores.**
615 Examples of serial EM images of phagophores at the disk (*A*), early-cup (*B*), middle-cup
616 (*C*), and late-cup (*D*) stages. The red arrows indicate phagophores. The numbers represent
617 the order of the serial images; scale bar, 1 μm.

618

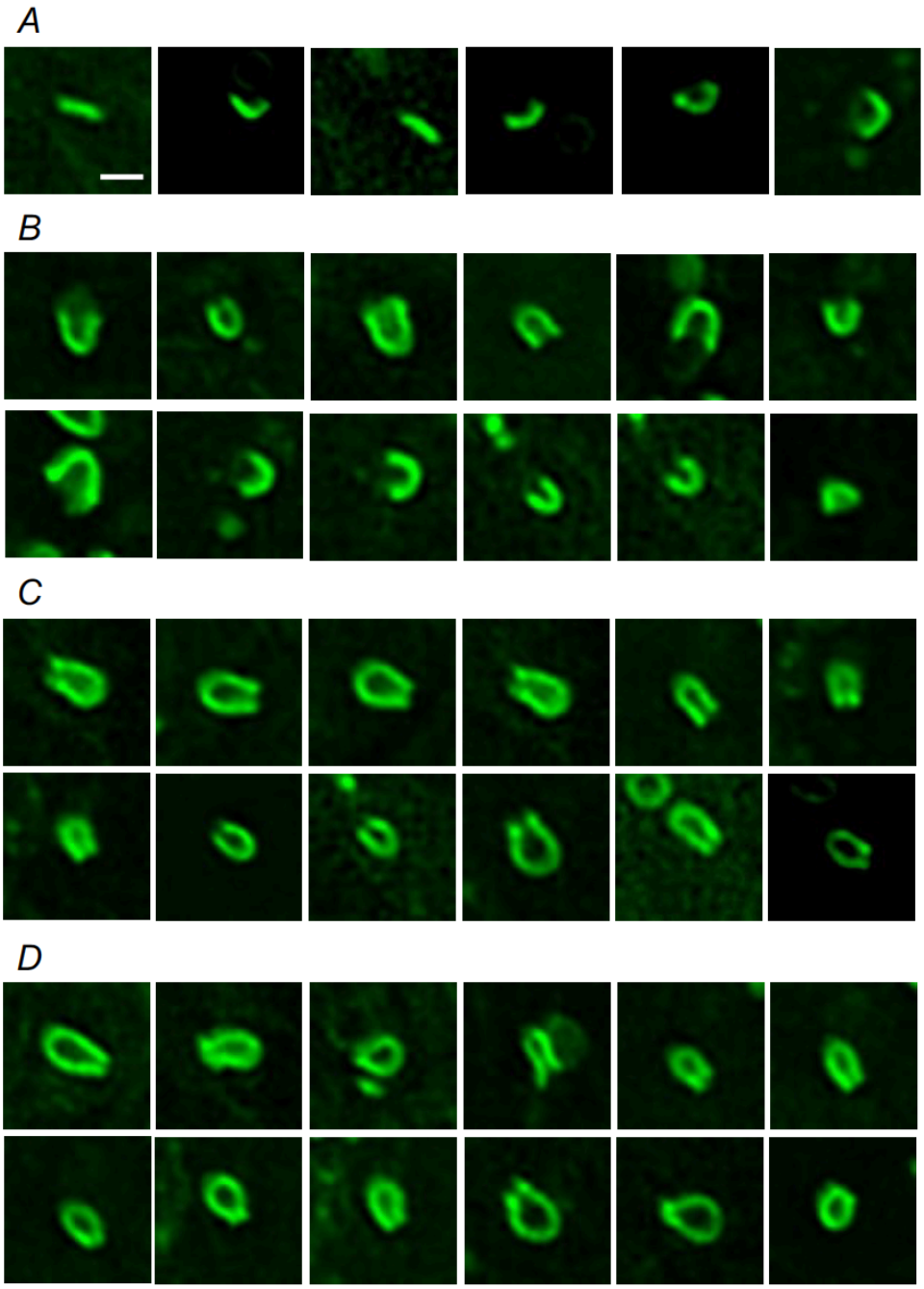

Figure S2. In vivo fluorescent images of phagophores.

Live-cell imaging of mouse embryonic fibroblasts expressing GFP-LC3B under starvation conditions; scale bar, 1 μm. Snap-shot images of phagophores were classified into disks (*A*), early-cups (*B*), middle-cups (*C*), and late-cups (*D*).

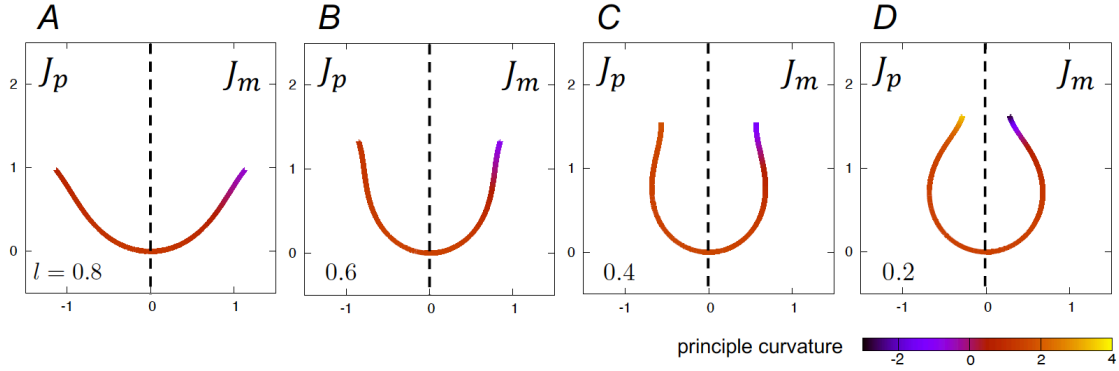

Figure S3. Two principle curvatures obtained from theoretical calculations. The meridional and parallel curvatures J_m and J_p are shown in the right ($x \geq 0$) and left ($x \leq 0$) regions, respectively. The same shapes as in Figure 6 were used. The unit of length was non-dimensionalized by the length $\sqrt{A/2\pi}$.

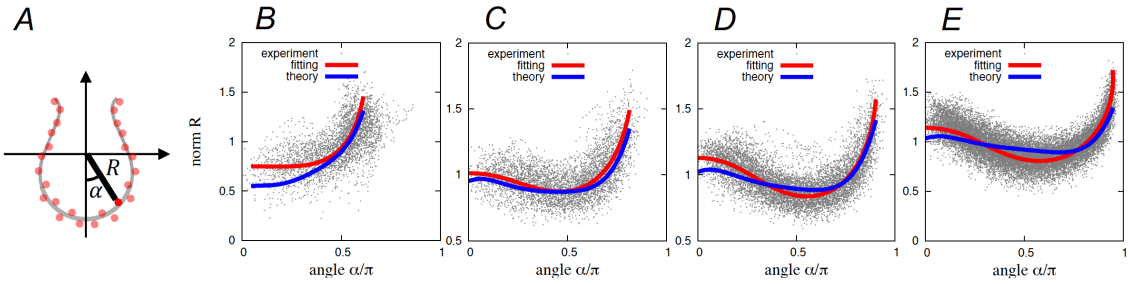

Figure S4. Comparison between experimental and theoretical results.
(*A*) The norm R and angle α, as polar coordinates, are shown. (*B–E*) Angular dependence of the norm R in the polar coordinate representation of disk (*B*), early-cup (*C*), middle-cup (*D*), and late-cup (*E*) shapes. The gray dots and the red lines represent the experimental point clouds and the fitting curves (R_{fit}), respectively. The data are the same as those used in Figure 4 (*A–D*). The blue lines represent the theoretical results (R_{theo}) in polar coordinates in Figure 6. The length unit of the norm was the same as in Figure 6. The relative errors between experimental and theoretical values ($|R_{theo} - R_{fit}|/R_{fit}$) for each shape were 29%, 20%, 20%, and 27%, respectively.

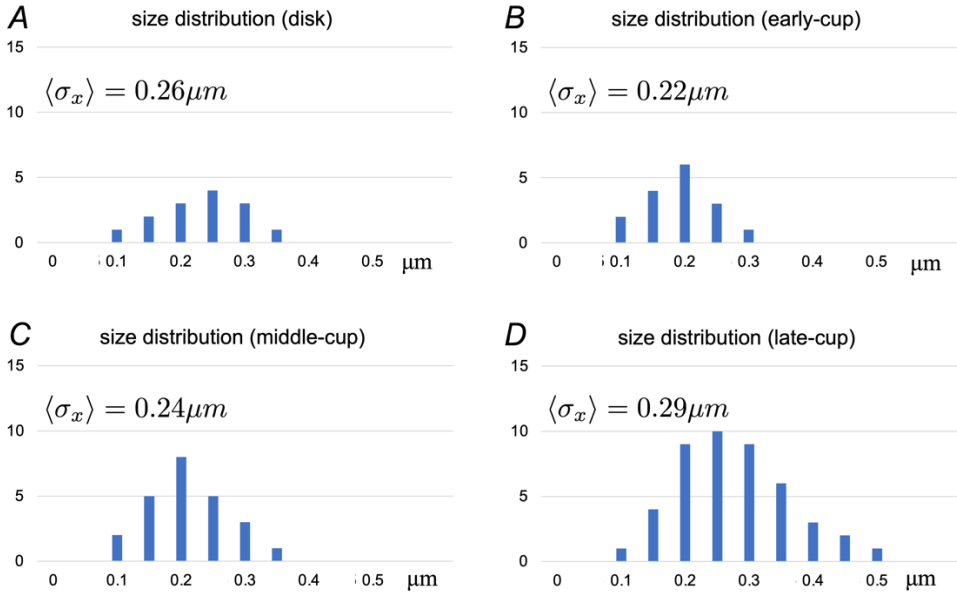

Figure S5. Distribution of deviations of point clouds of phagophores.
Histogram of the deviation of the point set, representing the size of the shape, for disks (*A*), early-cups (*B*), middle-cups (*C*), and late-cups (*D*). $\langle\sigma_X\rangle$ is the average value for each shape.

Video S1. Example of a rotating phagophore structure, corresponding to Figure 2D.

Video S2. Rotating view of the superposed disk morphology of a phagophore, corresponding to Figure 3A.

Video S3. Rotating view of the superposed early-cup morphology of a phagophore, corresponding to Figure 3B.

Video S4. Rotating view of the superposed middle-cup morphology of a phagophore, corresponding to Figure 3C.

Video S5. Rotating view of the superposed late-cup morphology of phagophore, corresponding to Figure 3D.

	a	b	c	d	χ_v^2
Disk	1.92 (0.16)	1.88 (0.19)	1.61 (0.09)	0.89 (0.11)	0.041
Early-cup	0.42 (0.02)	-0.49 (0.01)	0.06 (0.01)	0.91 (0.02)	0.018
Middle-cup	0.307 (0.006)	-0.587 (0.005)	-0.263 (0.005)	0.840 (0.003)	0.015
Late-cup	0.266 (0.003)	-0.464 (0.003)	-0.383 (0.004)	0.802 (0.002)	0.016

Table 1. Parameters of the fitting function for point clouds obtained from electron microscopy (EM) images.

The parameter sets of the polynomial function (Equation 5) that fit the point cloud shown in Figure 3*E–H*. The standard errors are in parentheses. The reduced chi-square (χ_v^2), which represents the goodness of fit, is also shown. The shapes obtained from each polynomial function are shown in Figure 4*A–D*.